Tribocorrosion behavior of β-type Ti-Nb-Ga alloys in a physiological solution

Ludovico Andrea Alberta [a,*], Jithin Vishnu [a], Yohan Douest [b,c], Kevin Perrin [c], Ana-Maria Trunfio-Sfarghiu [d], Nicolas Courtois [b], Annett Gebert [a], Benoit Ter-Ovanessian [c], Mariana Calin [a]

[a] Institute for Complex Materials, Leibniz Institute for Solid State and Materials Research Dresden (IFW Dresden), Helmholtzstr. 20, D-01069 Dresden, Germany
[b] Anthogyr SAS, F-74700 Sallanches, France
[c] Univ. Lyon, INSA de Lyon, MATEIS, UMR CNRS 5510, 69621 Villeurbanne, France
[d] Univ. Lyon, INSA de Lyon, LaMCoS, UMR CNRS 5259, 69621 Villeurbanne, France

ARTICLE INFO

ABSTRACT

Tribo-electrochemical behavior in physiological solution of two β-type (100-x)(Ti-45Nb)-xGa (x = 4, 8 wt%) alloys, alongside β-Ti-45Nb and medical grade Ti-6Al-4V ELI, was investigated. Microstructure and mechanical behavior were evaluated by X-ray diffraction, microhardness and ultrasonic method. Tribocorrosion tests (open circuit potential, anodic potentiostatic tests) were performed using a reciprocating pin-on-disk tribometer under constant load. Degradation mechanisms are similar for the alloys: plastic deformation, delamination, abrasive and adhesive wear. Among the β-Ti-Nb alloys, an improved wear resistance with lower damage was remarked for β-92(Ti-45Nb)-8Ga alloy, attributed to increased microhardness. Content of Ga^{3+} ions released in the test solutions were found to be in very low amounts (few ppb). Addition of Ga to Ti-45Nb resulted in improved corrosion resistance under mechanical loading.

1. Introduction

Titanium (Ti) and its alloys are extensively used in the biomedical field due to their high strength-to-weight ratio, excellent corrosion resistance and biocompatibility, mainly due to the spontaneous formation of a stable thin passive oxide film. Ti-6Al-4V (α + β) is a well-established metallic biomaterial for orthopedic and dental implant applications. However, its high Young's modulus ($E \cong 115$ GPa) may favor stress-shielding due to a large mismatch with the stiffness of living tissues and the toxicity of the alloying elements Aluminium (Al) and Vanadium (V) can represent a serious clinical concern in cases where large amounts of ions are released [1,2]. Research has recently focused on the development of novel β-type Ti alloys containing non-toxic elements such as Niobium (Nb), Molybdenum (Mo), Zirconium (Zr) and Tantalium (Ta) [3]. Ti-Nb based alloys are versatile candidates for biomedical applications for a number of reasons, including a low Young's modulus, high phase stability, good workability and ductility and outstanding

corrosion resistance and biocompatibility [4–7]. Further, Ti and Nb have a beneficial effect on the alloy corrosion resistance, and eventual release of metal ions is reduced as the stable barrier-type passive films provide protection to the underlying implant material [8]. Additionally, β-TiNb alloys in the solution-treated state exhibit low Young's modulus ($E \cong$ 60 GPa) [9], closer to that of human cortical bone ($E_{bone} \cong$ 10–32 GPa), thus decreasing the risk of the stress shielding phenomenon, which is caused by a large mismatch between the stiffness of the implant and of the surrounding bone tissues. In spite of the biocompatible compositions, improved corrosion resistance and low modulus, the serious aspects limiting the efficacy of Ti alloys for biomedical applications are poor wear resistance in body fluids and inability to prevent bacterial infection during early stages of recovery [10]. The latter can be tackled by alloying with antibacterial elements such as Copper (Cu), Zinc (Zn), Silver (Ag), Gallium (Ga) [11]. Ga recently gained attention due to its attractive antimicrobial properties [12]. Cochis et al. [13] have demonstrated that minor additions of Ga (1–2 wt%) to Ti alloys

demonstrate a highly efficient time-increasing antibacterial activity without any cellular toxicity. Our group recently reported the beneficial effect on the mechanical behavior of Ga addition to β-TiNb alloys, which resulted in improved strength while maintaining a low Young's modulus (78 GPa) [14].

Mechanically-assisted corrosion phenomena, such as tribocorrosion, critically affect the passive oxide film integrity, thereby accelerating material degradation. Even though Ti and its alloys are considered advantageous for implant applications, because of their biochemical characteristics, wear and corrosion still occur, especially in extreme environments like the human body [15]. Implants inserted in a human body encounter a particularly aggressive environment, being surrounded by body fluids for which chloride, dissolved oxygen and pH levels are critical from a corrosion perspective. The capacity of the oxide film to regenerate itself plays a key role in further determining the corrosion behavior of the implant; the sooner the film is repaired, the lower the amount of metal ions released in the body. Metallic ion release during tribocorrosion is critical as it can adversely affect the mechanical integrity as well as the biocompatibility [16]. Low wear resistance is also responsible for the appearance of wear debris, the accumulation of which in periprosthetic tissues can result in osteolysis and subsequent aseptic loosening [17]. Studies have shown that wear particles from Ti-6Al-4V alloys could induce the release of inflammatory mediators affecting the tissues surrounding prosthesis and cause osteolysis [18]. Corrosion behavior of β-Ti alloys is mainly governed by the role of the β-stabilizing agents on the oxide film. For example, a beneficial effect on the passivation behavior has been observed for Nb, attributed to its capacity of reducing anion vacancies in the oxide film, mainly composed of Ti- and Nb-oxides [19]. Extensive studies exist on the wear behavior of Ti-6Al-4V in both dry and wet conditions [20–22], but only limited wear data is available for β-type Ti-Nb-based alloys [23–25]. Furthermore, the synergistic interplay between corrosion and wear is often overlooked for such alloy systems. Because of the complexity of involved phenomena, the mechanisms of corrosion and wear due to specific combinations of materials, loadings and environments can be challenging to predict, therefore experimental studies are needed.

This work is part of an extended study focused on the development of antibacterial Ti-Nb-based alloys for load-bearing implant applications [14,26]. The novelty of the present study lies in reporting the tribocorrosion behavior of low modulus Ga-bearing β-TiNb alloys, namely (100-x)(Ti-45Nb)-xGa (x = 4, 8 wt%), alongside with Ti-6Al-4V ELI (grade 23) and Ti-45Nb, in physiological phosphate-buffered saline solution (PBS). The variations in open circuit potential, anodic current and friction coefficient as a function of time were measured in situ. Resulting wear tracks reveal the prevalent wear mechanisms. X-ray diffraction (XRD), ultrasonic and microhardness studies were performed to correlate phase composition and mechanical behavior to the observed electrochemical response under mechanical loading. Modelling was based on existing wear-accelerated corrosion models, and they accurately predicted the tribo-electrochemical response of the studied alloys. This work is fundamental in assisting the screening of candidates for next-generation implant biomaterials.

2. Materials and experimental methods

2.1. Preparation of the alloys, phase analysis and mechanical properties

Four different alloys are investigated in this work: medical grade Ti-6Al-4V Extra Low Interstitials (ELI, ASTM F136 grade 23), Ti-45Nb, 96 (Ti-45Nb)-4Ga and 92(Ti-45Nb)-8Ga. All compositions are given in wt %. Ti-6Al-4V ELI in form of disks was provided by Anthogyr SAS. Ti-45Nb was purchased from ATI - Specialty Alloys & Components. The two (100-x)(Ti-45Nb)-xGa alloys were prepared by arc melting and cold crucible casting from Ti-45Nb (99.9%, ASTM B348–13 grade 36) and high purity (99.99%) metallic Ga (purchased from Haines & Maassen Metallhandelsgesellschaft mbH). Ti-6Al-4V ELI was used as received,

while the other three alloys were subjected to a homogenization treatment (1000 °C, 24 h, in Ar atmosphere) followed by water quenching with the aim of preparing a chemically uniform state. Detailed description of these procedures can be found elsewhere [14].

Phase analysis of the alloys was carried out with a STOE Stadi P diffractometer in transmission geometry using Mo $K_{\alpha 1}$ (λ = 0.7093 Å) monochromatic radiation operated at 50 kV and 30 mA. Identification of crystalline phases is based on data from the International Centre of Diffraction Data (ICDD) PDF2 database (ICDD no-04–017–4957, β-Ti, and ICDD no-00–005–0682, α-Ti). For this reason, samples were mechanically ground to approximately 50 μm in thickness. Specimens for SEM observations were embedded in cold-hardening resin and subsequently mechanically polished by standard metallographic techniques.

Vickers microhardness ($HV_{0.1}$) was measured with an HMV-2 Shimadzu indenter on mirror-like polished samples with a force of 1 N (100 gf) and dwell time of 10 s. Average values and deviations are the result of 12 readings. Young's modulus (E) and Poisson's ratio (ν) of the bulk alloys were determined with a computer-controlled ultrasonic pulser-receiver device (Olympus 5900PR) on mechanically ground disks (Ø = 10 mm, thickness = 1.0 ± 0.2 mm). The setup allows the determination of normal and shear velocities of sonic waves by using two high frequency transducers (100 MHz and 20 MHz). The sonic waves are then related to the elastic properties E and ν [27]. Density (ρ) of the alloys was measured by Archimedes' method. All data are presented as mean ± standard deviation.

2.2. Corrosion and tribocorrosion tests

Disk-shaped (Ø = 10 mm, thickness $\sim$ 2 mm) specimens for electrochemical studies were embedded in epoxy resin, mechanically ground with SiC emery paper (from 240 to 2400 grit) and then ultrasonically rinsed in pure ethanol. After that, samples were stored for 24 h in natural air conditions to stabilize the native passive film.

A three-electrode setup was used for corrosion and tribocorrosion assessment. The setup consisted of the embedded Ti-based specimen as working electrode (WE), a platinum coil as counter electrode (CE) and a saturated silver chloride (Ag|AgCl) electrode as RE ($E_{Ag|AgCl}$ = +0.197 V vs SHE). The total volume of electrolyte was 14 (± 0.03) mL. The setup as described was connected to a Gamry ref 600 potentiostat, which was controlled using Gamry Framework software. The electrochemical configuration was suitable to the measurement of the OCP as well as of the current under dynamic potential (potentiodynamic test) and fixed potential (potentiostatic test), with or without sliding under mechanical loading. All tests were conducted in air-saturated physiological phosphate-buffered saline solution (PBS, pH $\sim$ 7.4, composition: NaCl 140 mM, KCl 3 mM, phosphate buffer 10 mM, purchased from Merck KGaA) at room temperature.

2.2.1. Corrosion tests in absence of wear

Corrosion behavior was studied by standard electrochemical techniques: OCP monitoring followed by dynamic polarization. Open circuit potential (OCP) was monitored for 3600 s before the polarization. The linear dynamic anodic polarization was started at − 0.2 V below the last OCP potential value (−0.2 V vs OCP) and increased with a constant sweep rate of 0.5 mV/s up to a value of + 1.0 V vs. Ag|AgCl. Each test was performed at least three times to verify the repeatability of the results. By graphical extrapolation, the characteristic corrosion parameters (E_{corr}, j_{corr} and j_{pass} at +1 V vs. Ag|AgCl) were determined from the curves.

2.2.2. Tribocorrosion tests

Sliding tests were performed with a reciprocating pin-on-disk tribometer. The tribometer has a fixed frame that holds the pin support, while the stage holding the electrochemical cell is mobile (Fig. 1). The translation movements and load, fixed at 5 N, were applied using a lifting table (Norelem). Normal load and shear force were measured by a
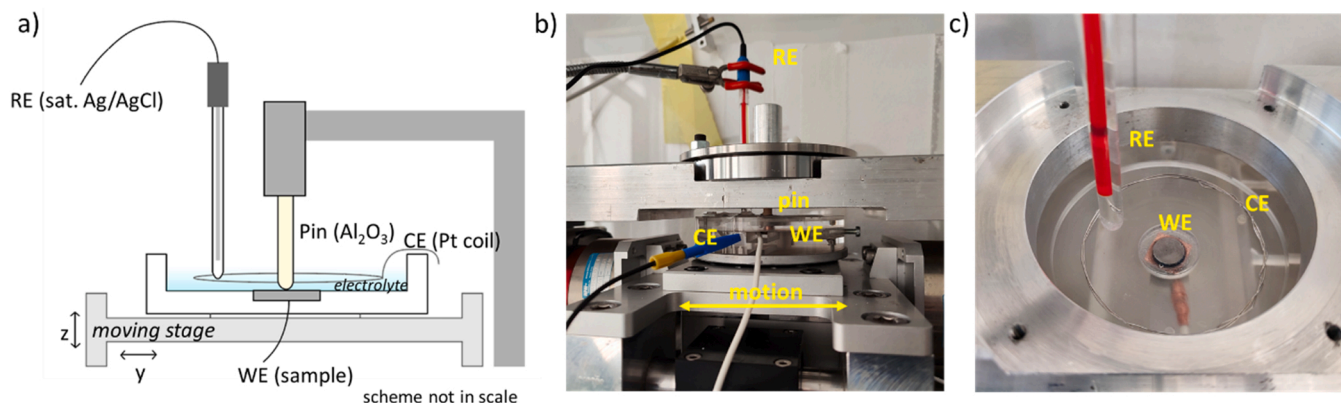
Fig. 1. (a) Scheme of the tribo-electrochemical setup, (b) side view and (c) top view (without pin holder).

three-axis strain gauge force sensor (Testwell). On top of the sensors, the whole electrochemical cell was mounted and fixed in position. The coefficient of friction (COF) was calculated by the ratio between shear force and normal force. The horizontal displacement was driven by a linear voice coil actuator (H2W Technologies). Sliding displacement was set to 1.6 mm with a reciprocating frequency of 0.5 Hz for 1800 s (2 s/cycle, which corresponds to 3.2 mm/cycle) and sinusoidal waveform profile. This leads to an experimental total sliding distance of 2.9 m for each test. The tribometer was controlled by LabVIEW (National Instruments) software, which allows real time visualization of normal force, tangential force and horizontal displacement [28].

The contact was defined by the Ti alloys as first body and a cylindrical (Ø = 6 mm) alumina (Al_2O_3) pin with a curvature radius of 26 mm (measured by profilometry) as second body. This type of ceramic pin was selected in order to limit severe adhesive wear which typically occurs during metal-metal contact [29]. Moreover, mechanical properties of the Al_2O_3 pin are higher than the tested Ti alloys, therefore wear was exclusively expected on the metal specimens. The pin was polished with SiC emery paper (grit 4000) before every test with an in-house built pin holder, designed to maintain the same curvature radius. Mechanical properties of the pin are reported elsewhere [30]. According to Hertz's elastic theory, calculations give initial maximum contact pressures of 240, 180, 190, 200 MPa and mean contact pressures of 160, 120, 130, 130 MPa for Ti-6Al-4V ELI, Ti-45Nb, 96(Ti-45Nb)-4Ga and 92 (Ti-45Nb)-8Ga, respectively. Chosen contact mechanics conditions are far from real joint replacement biomechanics, where contact pressures for hip joints, ankle replacements and knee joints are in the range of few tens of MPa [28]. Chosen conditions may therefore seem harsh but are needed for a fundamental mechanistic study.

The tribometer operated integrated with the electrochemical setup described above. Two types of tribo-corrosion tests were carried out: i) sliding during OCP monitoring and ii) sliding at applied anodic potential (0 V vs last measured OCP potential). The first method simulates a real system, where the WE potential is controlled only by the physiochemical properties of the surrounding solution and the tribological conditions of the contact. The second method allows real time in situ measurement of depassivation and repassivation kinetics. Tests described below were repeated twice for reproducibility.

i. **Open circuit potential (OCP) measurements**: Initially, OCP was monitored in static conditions for 3600 s, and subsequently with sliding for 1800 s to gain insights on the OCP evolution under the applied 5 N load. Sliding was then stopped and OCP was further measured for 3600 s. Data collection frequency was set to 10 Hz to ensure high resolution curves during sliding tests.

ii. **Potentiostatic tests**: After OCP stabilization for 3600 s, potentiostatic experiments were performed at an applied anodic potential of 0 V vs OCP to understand the mutual action of corrosion and wear

during tribocorrosion. This indicates that the last measured OCP potential value at 3600 s after OCP monitoring was chosen as applied potential for the subsequent potentiostatic test. Initially, current measurements were carried out without sliding for 300 s, after which sliding took place for 1800 s. Sliding was then stopped and current was monitored for 600 s more.

2.3. Ex-situ surface characterization of wear tracks

Wear tracks morphologies were observed with a Zeiss Leo Gemini 1530 scanning electron microscope (SEM) operated at an accelerating voltage of 20 kV. Total wear volume (V_{tot}) and depth (D) were evaluated with a non-contact S Neox 3D confocal optical profiler equipped with a 20X Nikon - EPI objective (resolution: 0.65 µm/pixel), driven by Sensomap standard (v. 6.7) software. The process to compute volume loss consists of four steps:

i. the 3D topography of wear track and surrounding plane surface is measured,
ii. a mathematical reference plane is constructed from a least-square fit of the plane surface around the wear track,
iii. non-measured empty points are refilled by nearest neighbors smoothing,
iv. the total wear volume is computed by subtracting the wear track topography from that of the modelled plane surface.

2.4. Quantification of wear

In a tribocorrosion system, many degradation mechanisms take place simultaneously contributing to material loss. According to Mischler's model [31–33], the overall material degradation or volume loss (V_{tot}), is caused by a combination of mechanical removal (V_{mech}), wear-accelerated corrosion (V_{wac}) and corrosion outside the wear track (V_{corr}). The latter can be assumed negligible in passive alloys such as Ti-Nb-based alloys [5,34], therefore the overall material loss can be expressed as follows:

$$V_{tot} = V_{mech} + V_{wac} \quad (1)$$

Volume loss due to wear-accelerated corrosion (V_{wac}) can be determined from the average current during wear (i_{wear}) by using Faraday's law (Eq. 2). According to this formula, the excess current (i_{exc}) produced by sliding at a passive potential corresponds to an equivalent oxidized metal volume (V_{wac}):

$$V_{wac} = \frac{i_{exc} \bullet t_{rub} \bullet M_{mol}}{n \bullet F \bullet \rho} \quad (2)$$

Where i_{exc} [A] is excess current, t_{rub} [s] is sliding time (always 1800 s), M_{mol} [g mol^{-1}] is the molar mass of the alloy, n is charge number, F is

Faraday's constant (96,485.3 C mol^{-1}) and ρ [g cm^{-3}] is density. Excess current i_{exc} was determined by subtracting the initial current (before sliding) from the value of i_{wear}. This calculation is needed to eliminate the contribution of eventual current coming from outside the wear track, which is negligible as mentioned earlier. The average i_{exc} coming from two independent tests is used for determination of V_{wac}. The charge number (n) was calculated from the alloy atomic ratio by assuming the following oxidation states of 4, 5, 3 for Ti, Nb, Ga and 3 and 5 for Al and V, respectively. Excess current i_{exc}, and therefore volume loss due to wear-accelerated corrosion in OCP conditions, can also be determined according to the galvanic cell model proposed by Vieira et al. [35]. Corrosion potential of the alloys determined by polarization tests in absence of wear, cathodic kinetics, potential attained during sliding and anode-to-cathode area ratio are considered for the calculation of the anodic current flowing through the wear track:

$$\log i_{exc} = \frac{E_{corr} - E_{wear} + B_c}{B_a} - \log\left(\frac{A_a}{A_c}\right) \qquad (3)$$

where E_{corr} is the corrosion potential, E_{wear} is the potential measured during rubbing, B_c and B_a are Tafel constants graphically extracted by linear regression from the polarization curves. A_a corresponds to the anode area (wear track), determined *ex situ* by 3D confocal microscopy, A_c corresponds to the cathode area, which can be approximated by the sample surface area. The total wear volume (V_{tot}) was determined by 3D confocal microscopy. Therefore, it becomes possible to calculate the mechanical wear (V_{mech}) due only to the sliding action from Eq. 1 by subtracting the chemical losses from the total losses.

2.5. Metal ion release after tribocorrosion tests

The metal ion concentration in the electrolyte solutions after the tribocorrosion tests was measured by Inductively Coupled Plasma - Mass Spectrometry (ICP-MS) using an iCAP TQe (ThermoFisher) instrument. For this purpose, the solutions coming from the sliding tests under OCP conditions were retrieved by pouring the electrochemical cell content into sterile plastic containers. For the analyses, 500 µL of test solution were mixed with 49.5 mL of a nitric acid HNO$_3$ solution (2–4% v/v), such dilution is chosen to minimize non-spectroscopic interference coming from easily ionizable ions such as Sodium (Na) and Potassium (K), present in very large concentrations in the electrolyte. Rhodium at 500 ppb is used as an internal standard to correct for non-spectroscopic interference. The metal ions analyzed were Ti-48, Nb-93 and Ga-71, which have detection limits of 21 ppt, 10 ppt and 2.7 ppt, respectively. Fresh PBS solution was also measured as blank. Tests were repeated twice, with solutions coming from two independent sliding tests.

3. Results

3.1. Microstructure and mechanical properties

XRD diffractograms of Ti-45Nb, 96(Ti-45Nb)-4Ga, 92(Ti-45Nb)-8Ga and Ti-6Al-4V ELI are shown in Fig. 2a. It is evident that the three Ti-Nb-based alloys consist of a single bcc β-phase, suggesting that all elements are in solid solution, while Ti-6Al-4V ELI shows reflections belonging to both hcp α- and bcc β-phases. SEM studies reveal equiaxed β-grains for the three TiNb-based alloys and a biphasic microstructure consisting of elongated grains for Ti-6Al-4V ELI [36]. Further details about micro-structural features of these β-type alloys can be found elsewhere [14,26]. Vickers microhardness ($HV_{0.1}$) values are listed in Table 1. The lowest microhardness is obtained for the reference Ti-45Nb alloy (147 $HV_{0.1}$), then it increases with Ga addition to 226 $HV_{0.1}$ (Ga 4 wt%) and 232 $HV_{0.1}$ (Ga 8 wt%). The greatest microhardness is observed in α + β-Ti6Al-4V alloy (354 $HV_{0.1}$), in agreement with what is generally reported [37]. Young's modulus (E) of the bulk alloys was measured by means of ultrasonic pulse-echo method. Results, together with other properties of the alloys are listed in Table 1. The reference β Ti-45Nb alloy shows the lowest E value of 63 GPa, while the α + β-Ti6Al-4V alloy exhibits the highest value of approximately 111 GPa. The developed β-type 96(Ti-45Nb)-4Ga and 92(Ti-45Nb)-8Ga alloys exhibit E values of 69 and 79 GPa respectively, such increase could be exerted by the presence of Ga atoms in the bcc lattice. These findings are well in agreement with those reported for similar α + β- and β-alloys [6,8,38].

3.2. Corrosion tests in absence of wear

Conventional polarization tests to study general corrosion behavior in absence of wear are carried out before the actual tribocorrosion tests. The potentiodynamic polarization curves without sliding of Ti-45Nb, 96(Ti-45Nb)-4Ga, 92(Ti-45Nb)-8Ga and Ti-6Al-4V ELI are shown in Fig. 3. All four Ti alloys show very similar corrosion characteristics. Corrosion potentials (E_{corr}) of the three Ti-Nb-based alloys are in the range of $-485 \div -378$ mV vs. Ag|AgCl, suggesting a modest increase in noble behavior when Ga is added to Ti-45Nb. The observed corrosion current densities (j_{corr}) are low and agree well with literature [37,39,40]: 77 $\pm$ 14, 151 $\pm$ 11, 89 $\pm$ 10 and 107 $\pm$ 22 nA/cm^2 for Ti-6Al-4V ELI, Ti-45Nb, 96(Ti-45Nb)-4Ga and 92(Ti-45Nb)-8Ga, respectively. The anodic branch of the curves shows a passive region associated with the
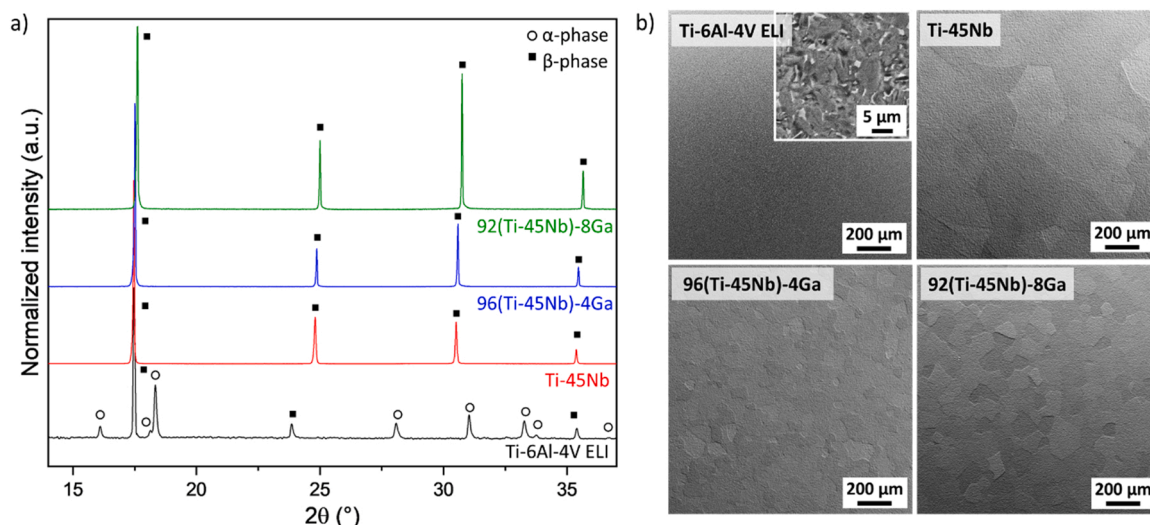

Fig. 2. (a) XRD diffraction patterns and (b) SEM micrographs of investigated alloys.

Table 1

Microstructure and relevant properties of the alloys under investigation in the present study.

Alloy	Microstructure	Density ρ (g/cm^3)	Molar mass M_{mol} (g/mol)	Charge number n	Young's modulus E (GPa)	Vickers microhardness $HV_{0.1}$	Poisson's ratio ν
Ti-6Al-4V ELI	$\alpha + \beta$	4.45	45.8	4.02	110.8 ± 0.1	354 ± 6	0.333 ± 0.001
Ti-45Nb	β	5.67	61.0	4.29	63.0 ± 0.1	147 ± 3	0.415 ± 0.002
96(Ti-45Nb)-4Ga	β	5.76	61.5	4.25	69.4 ± 1.5	226 ± 3	0.404 ± 0.006
92(Ti-45Nb)-8Ga	β	5.78	61.8	4.20	79.1 ± 0.9	232 ± 5	0.391 ± 0.002
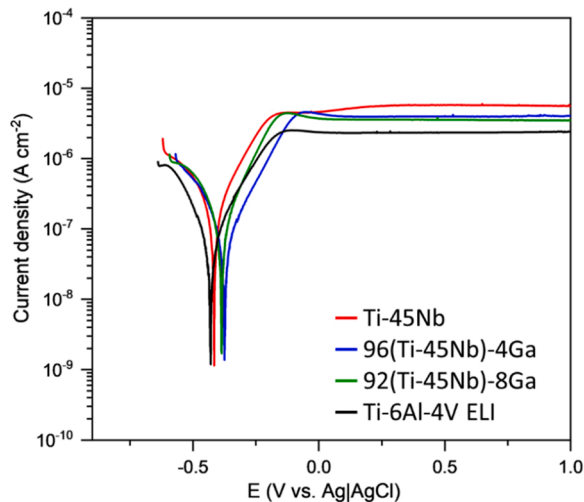
Fig. 3. Potentiodynamic curves recorded at a scan rate of 0.5 mV/s of the four alloys in PBS solution after OCP adjustment of 3600 s (For interpretation of the references to color in this figure legend, the reader is referred to the web version of this article.).

formation of the protective film. After the anodic oxidation step, a stable passive regime can be observed up to + 1 V vs. Ag|AgCl for the four alloys, indicating no potential breakdown and high stability of the film. Modest differences can be observed in the passive current densities (j_{pass}) at + 1 V vs. Ag|AgCl, where the highest j_{pass} is observed for the reference Ti-45Nb (5.51 ± 0.16 μA/cm^2), then decreases in the order 96(Ti-45Nb)-4Ga and 92(Ti-45Nb)-8Ga (4.38 ± 0.35 and 3.48 ± 0.04 μA/cm^2, respectively), and the smallest j_{pass} for Ti-6Al-4V ELI (2.47 ± 0.07 μA/cm^2). These results suggest a slightly more reactive surface for the reference Ti-45Nb, and less reactive when Ga is added, pointing towards the role of Ga incorporation in modifying the passive film properties.

3.3. Tribocorrosion tests at OCP

The evolution of the open circuit potential (OCP) over time of the four titanium alloys is monitored before, during and after sliding (Fig. 4a); electrochemical parameters are summarized in Table 2. Three main regions can be detected. The first region, until 3600 s, shows the stabilization of the OCP potential. Before the onset of sliding, the measured OCPs for all the alloys are stable, with nobler potential exhibited by both 96(Ti-45Nb)-4Ga and 92(Ti-45Nb)-8Ga. At 3600 s, the second region can be observed, where sliding occurred by applying a nominal normal load of 5 N. All four alloys exhibit a substantial and abrupt decrease in the potential value, which is the typical tribocorrosion behavior for passive metals and alloys. This occurs due to the local mechanically-accelerated breakdown of the passive film (depassivation process). This negative shift indicates the initiation of local electrochemical activity, during which the fresh bare metallic surface is exposed to the chloride-rich corrosive environment, and therefore starts

to react. In general, during sliding, tribological stresses lead to the removal of the passive film on the real contact areas between pin and metallic sample. This subsequently leads to the formation of highly reactive regions in the wear track, as compared to the surrounding region outside the wear area [41]. The potential value reached during sliding (E_{wear}) results from the galvanic coupling between the worn depassivated area (wear track), which acts as a local anode, and the surrounding large passive unworn area, which acts as a cathode [42]. The lowest drop in sliding potential during the onset of sliding is exhibited by Ti-6Al-4V ELI (420 mV), while the potential drop was comparatively higher for 96(Ti-45Nb)-4Ga and 92(Ti-45Nb)-8Ga (469 mV and 505 mV). The curves of the three β-Ti alloys appear noisier than the α + β-Ti-6Al-4V ELI in the initial region. The OCP curve of Ti-6Al-4V ELI changes from smooth to noisy after 600 s, which may indicate that the surface is subjected to cyclic depassivation and repassivation. The fluctuations in the potential observed in Ti-6Al-4V ELI are in between - 888 and - 739 mV vs Ag|AgCl. A very similar observation was made by Hacisalihoglu et al. [24] in an α + β-Ti-6Al-4V alloy tested in SBF solution, where the OCP curve under rubbing became very noisy after 600 s. The curves of Ti-45Nb and 96(Ti-45Nb)-4Ga exhibit a steady-state trend throughout the sliding, with potential oscillations in the range of ~ 100 mV indicating the establishment of a dynamic equilibrium between depassivation and repassivation processes. The 92(Ti-45Nb)-8Ga alloy shows an increasing drift trend from the moment sliding started, suggesting a tendency to spontaneously repassivate even during mechanical degradation and with less extent of depassivation. In the third region at 5400 s, sliding is stopped and the potential of all four alloys increases and reaches values closer to those of pre-sliding conditions in the case of Ti-6Al-4V ELI and slightly lower for the three β-Ti alloys, as a consequence of the reformation of the passive layer in the worn area. The post-sliding potentials could be related to the coverage of wear debris over the wear track and thickening of the passive film outside the wear track due to accelerated mass transportation during sliding [43]. The potential restoration process provides valuable information on the alloy ability to recover after wear. Time constants of repassivation (t_{repass}) are determined by graphical extrapolation as shown in Fig. 4c and reported in Table 2. From these results, it seems that the addition of Ga is beneficial to the repassivation kinetics with values decreasing from 24.1 to 17.3 s with increasing Ga content, while Ti-6Al-4V ELI shows the slowest repassivation with 27.9 s

3.4. Tribocorrosion tests at applied potential

The results of the tribocorrosion tests performed under potentiostatic conditions (0 V vs last OCP value, after 3600 s of OCP stabilization) are shown in Fig. 5 and relevant electrochemical parameters summarized in Table 3. This methodology was chosen so that the same surface conditions around the worn area are attained for each independent test. The applied potentials were in the range of − 300 and − 315 mV vs Ag|AgCl for all tests. At the applied potential, the whole Ti-based surfaces are initially passive and the measured current, before sliding, was below 10 nA. At the onset of rubbing, current sharply increases due to the mechanical detachment of the passive film [44]. During the sliding period, the local worn area is forced to an anodic regime, while the surrounding unworn areas retain their OCP condition. A steady-state
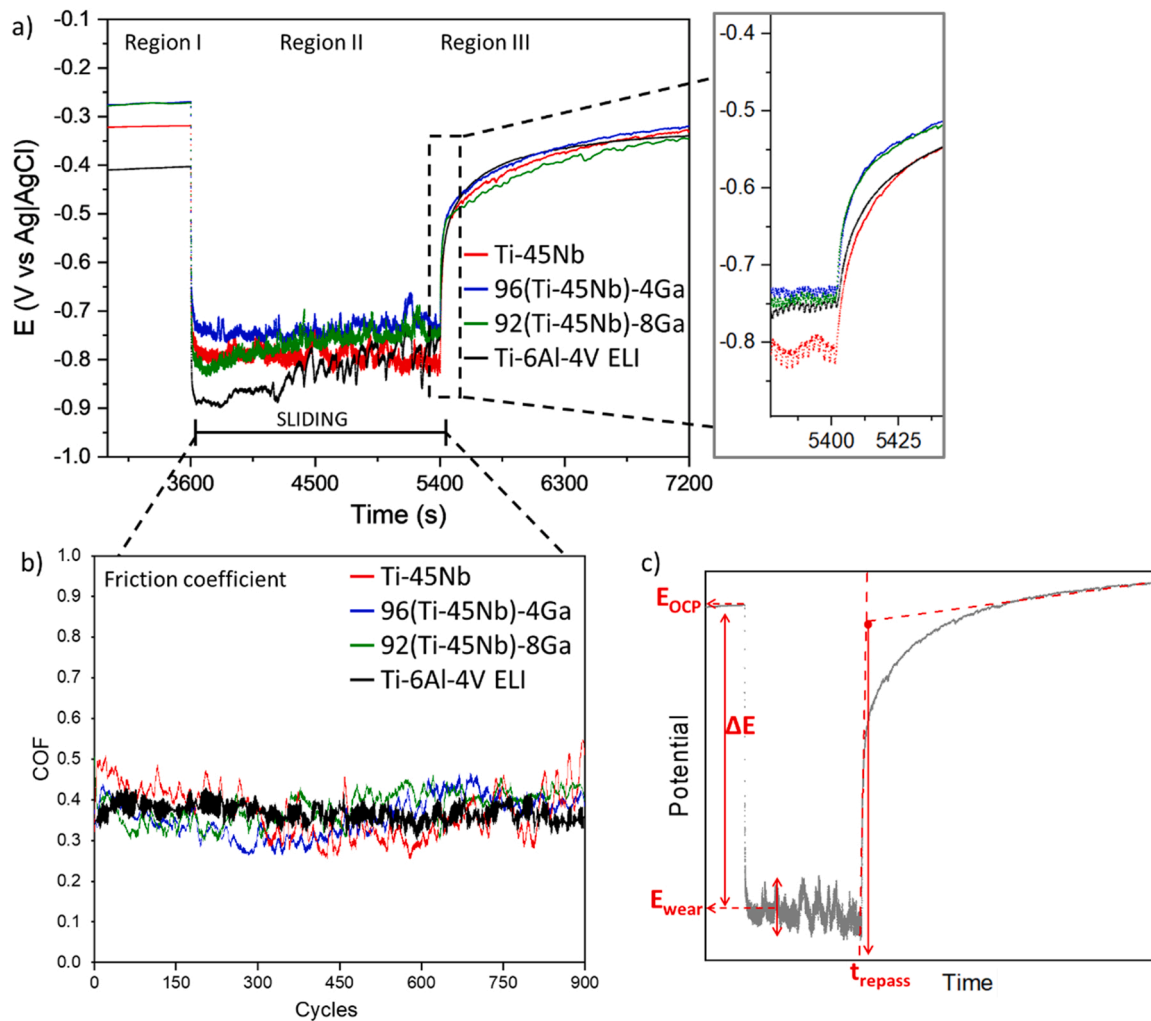
Fig. 4. (a) OCP evolution curves over time during sliding (load 5 N) of an alumina pin against the four Ti alloys in PBS; (b) evolution of friction coefficient (COF) over time (900 cycles correspond to 30 min), (c) schematic representation for the determination of the parameters: OCP value before sliding (E_{OCP}), average potential during sliding (E_{wear}), potential drop (ΔE), repassivation time constant (t_{repass}), reported in Table 2. (For interpretation of the references to color in this figure legend, the reader is referred to the web version of this article.).

Table 2
Electrochemical parameters determined from the OCP curves under sliding, as shown in Fig. 4c: potential before sliding (E_{OCP}), during sliding (E_{wear}), potential drop ($|\Delta E|$) and repassivation time constant (t_{repass}).

Alloy	Potential before sliding E_{OCP} (mV vs Ag|AgCl)	Potential during sliding E_{wear} (mV vs Ag|AgCl)	Potential drop $\|\Delta E\|$ (mV vs Ag|AgCl)	Repassivation time constant t_{repass} (s)
Ti-6Al-4V ELI	-406 ± 5	-826 ± 11	420 ± 16	27.9 ± 0.8
Ti-45Nb	-298 ± 29	-764 ± 35	466 ± 64	24.1 ± 0.5
96(Ti-45Nb)-4Ga	-267 ± 3	-736 ± 28	469 ± 31	20.3 ± 1.4
92(Ti-45Nb)-8Ga	-286 ± 21	-791 ± 34	505 ± 55	17.3 ± 1.5

mean value of current is observed for the four alloys throughout the course of the tests. However, great differences can be detected between Ti-6Al-4V ELI and the three β-Ti alloys. While for Ti-6Al-4V ELI anodic current is in the range of ~ 2 ÷ 50 μA, great fluctuations up to 200 μA can be observed for the three Ti-Nb-based alloys. Once sliding is interrupted at 2100 s, current immediately decreases by approximately two orders of magnitude, indicating almost instantaneous repassivation in the worn area. The lowest average current after sliding (i_{final}), mainly flowing through the wear track, is observed for Ti-6Al-4V ELI (0.06 ± 0.05 μA), the highest for Ti-45Nb (0.85 ± 0.63 μA), while the two (100-x)(Ti-45Nb)-xGa alloys exhibit intermediate similar values of 0.35

± 0.16 and 0.30 ± 0.19 μA, respectively. A satisfactory reproducibility of the current results with a maximum deviation of 9% from the average value was observed.

3.5. Analysis of worn surfaces

Morphology of the wear tracks was characterized by 3D optical profilometry and SEM, results are shown in Fig. 6. Microstructural investigations were carried out on wear tracks of samples measured under OCP conditions, which were strategically selected to study the effect of
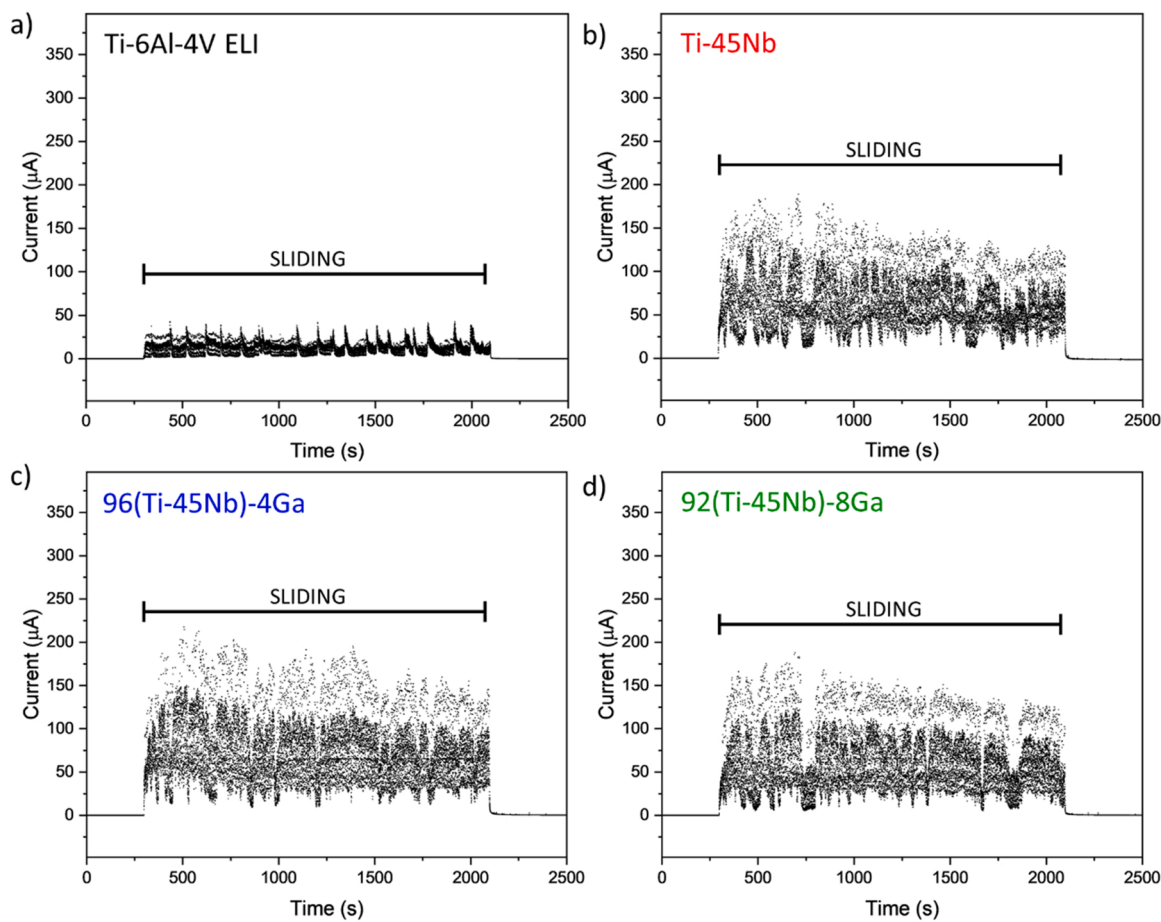
Fig. 5. Current evolution with time during sliding (load 5 N) with an alumina pin against (a) Ti-6Al-4V ELI, (b) Ti-45Nb, (c) 96(Ti-45Nb)-4Ga, (d) 92(Ti-45Nb)-8Ga at applied potential (0 V vs final OCP) in PBS solution.

Table 3
Electrochemical parameters determined from the potentiostatic curves of Fig. 5.

Alloy	Current during wear i_{wear} (µA)	Current after wear i_{final} (µA)
Ti-6Al-4V ELI	13 ± 7	0.06 ± 0.05
Ti-45Nb	65 ± 30	0.85 ± 0.63
96(Ti-45Nb)-4Ga	75 ± 35	0.35 ± 0.16
92(Ti-45Nb)-8Ga	61 ± 32	0.30 ± 0.19

the corrosive environment in presence of a tribological contact without the influence of any external potential. All images show plowing grooves of varying width, depth and length running parallel to the sliding direction. Rubbing scratches become deeper moving from the edge to the mid-width of the wear tracks. In order to quantitatively analyze and compare the tribological contacts, total wear volume (V_{tot}) and wear depth (D) were calculated from the 3D measurements (Table 4). It is evident how the four alloys show substantially different worn surfaces, especially between Ti-6Al-4V ELI and the three Ti-Nb-based alloys. The former exhibits not so deep scratches, with a depth (D) of 4.05 µm, while Ti-45Nb shows a very deep scar of 10.16 µm. These values are similar to those reported by Feyzi et al. [45] for a Ti-6Al-4V tested against a zirconia ball in PBS solution: they measured, by contact profilometry, a depth of ~ 10 µm for wear tracks produced by loads of 3.5 and 6 N. In terms of 92(Ti-45Nb)-8Ga, V_{tot} and D were respectively reduced of 49% and 44% compared to Ti-45Nb. No significant difference was observed in the computed geometric dimensions determined from samples subjected to the two types of electrochemical test.

SEM observations of the wear track patterns (Fig. 6e-p) can offer insights into the underlying mechanisms of wear and friction. It is

evident that the micrographs confirm the observed features present in the 3D profiles: visible grooves are evident along the sliding direction. As mentioned, a more severe abrasive wear can be confirmed for the reference Ti-45Nb, while Ti-6Al-4V ELI exhibits more superficial scratches, confirming its well-known wear resistance. Wear particles and debris resulting from severe deformation and tearing out (delamination) can be observed along the edge of grooves in all alloys. The extent of cutting abrasion is lesser for Ti-6Al-4V ELI compared to the three Ti-Nb-based alloys. The latter show wear debris (as indicated by yellow arrows in relevant images) in important amounts indicating delamination wear mechanism, ranging between a few hundred nanometers to approximately 5 µm (Fig. 6m-p). The large particles seem to be agglomerations of finer and smaller debris. The formation of such wear debris could act as third bodies capable of amplifying the wear during tribocorrosion. No damage of the counter body alumina pin could be observed by optical microscopy after the tests (Fig. S1), on the contrary, wear debris detached from the Ti samples and transferred to the pin can be detected, confirming adhesive wear. These results indicate that the wear resistance of the two (100-x)(Ti-45Nb)-xGa alloys situates between Ti-6Al-4V ELI and Ti-45Nb.

3.6. Friction and wear

Evolution of the friction coefficients (COF) over time during sliding was recorded simultaneously to the electrochemical signals of both test types. Representative curves are shown in Fig. 4b. Values remained constant around the average with greater fluctuations for the three Ti-Nb-based alloys compared to Ti-6Al-4V ELI, as reported in Table 4. Corroborating the changes in potential, oscillations in COF curves were
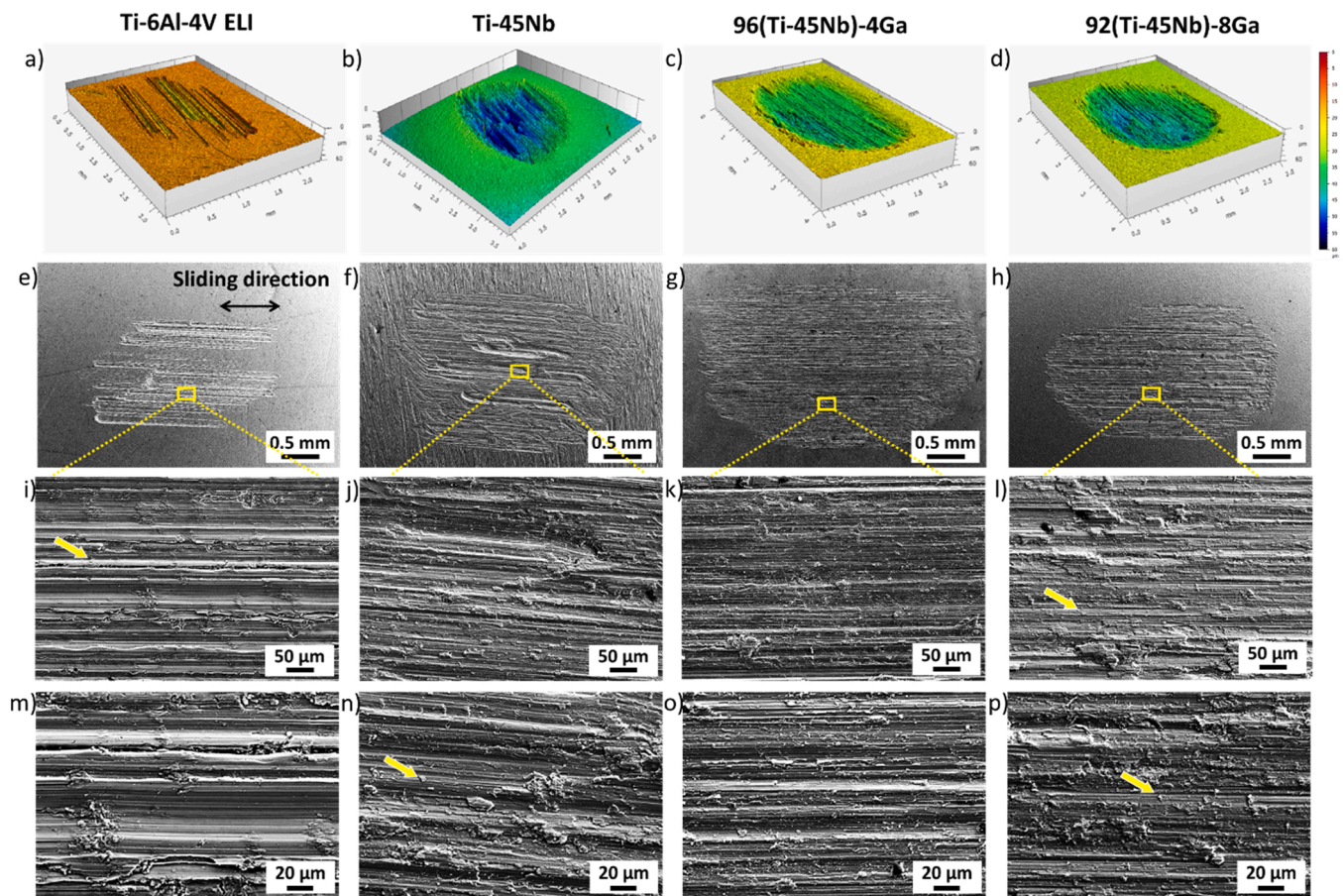
Fig. 6. Morphological features of the wear tracks under OCP conditions of the four tested alloys characterized by (a-d) 3D optical profilometry and (e-p) SEM. Squares in e-h represent areas of interest shown in i-p (sliding direction, valid for images e-p, is indicated by double arrow in image e). (For interpretation of the references to color in this figure legend, the reader is referred to the web version of this article.).

Table 4
Summary of the results extracted from the sliding tests. Total volume loss (V_{tot}) and depth of the wear track (D) were determined from 3D optical profilometry measurements. Volume losses due to wear-accelerated corrosion (V_{wac}) and to mechanical wear (V_{mech}) are determined as previously described. D and V_{tot} are the results of characterization of wear tracks coming from two independent tests. Average V_{tot} is used for the determination of V_{mech}.

Alloy	COF (dimensionless)	Depth D (μm)	Total volume loss V_{tot} x 10^{-3} (mm^3)	Volume loss due to wear-accelerated corrosion V_{wac} x 10^{-3} (mm^3)	Volume loss due to mechanical wear V_{mech} x 10^{-3} (mm^3)
Ti-6Al-4V ELI	0.40 ± 0.03	4.05 ± 0.84	10.41 ± 4.42	0.70 ± 0.09	9.71 ± 4.33
Ti-45Nb	0.40 ± 0.02	10.16 ± 1.05	54.41 ± 3.72	2.81 ± 0.34	51.60 ± 3.38
96(Ti-45Nb)-4Ga	0.42 ± 0.03	8.60 ± 0.17	52.74 ± 2.44	3.22 ± 0.40	49.52 ± 2.84
92(Ti-45Nb)-8Ga	0.38 ± 0.02	5.71 ± 0.11	27.90 ± 3.98	2.33 ± 0.82	39.86 ± 3.17

larger for β alloys as compared to Ti-6Al-4V ELI. No significant difference was observed in the values of COF determined at OCP or under applied anodic potential. Similar observations were made by Feyzi et al. [45] and concluded that the friction coefficient was independent of the imposed potential.

Table 4 also contains relevant data necessary to evaluate and quantify wear: chemical (V_{wac}) and mechanical (V_{mech}) contribution to total wear volume (V_{tot}) are determined according to Eqs.1–3, whereas V_{tot} and wear depth (D) are determined by 3D confocal profilometry.

Wear-accelerated corrosion (V_{wac}) under applied anodic potential represents around 6% of the total wear volume, while at OCP conditions, determined by the galvanic cell model [35], is less than 3%. This model was successfully applied by Guiñòn Pina et al. [25] to a series of

Ti-30 Nb-xSn alloys, where wear-accelerated corrosion at passive applied potentials represents around 5% of the total wear, while the contribution at OCP is less than 0.5%. The lowest volume loss was observed for the Ti-6Al-4V ELI alloy, while Ti-45Nb showed the highest. A significant decrease in the total wear volume can be noticed when Ga content is 8 wt%. These results indicate a limited contribution of wear-accelerated corrosion to the total wear, which is mainly determined by the mechanical sliding action.

3.7. Metal ions release after tribocorrosion

The metal ion content was measured in the solutions after sliding tests under OCP conditions. Applying a potential completely changes the

tribocorrosion conditions; in the case of an anodic potential, metal ion release significantly increases [46]. Concentrations of all scanned elements, i.e. Ti, Nb, Ga, were within the cytotoxicity limits reported by many authors [13,47,48] in fibroblasts and preosteoblasts progenitor cells. Interestingly, an increasing amount of Ga(III) release with Ga content in the alloys tested in the same conditions was detected in the solutions. The amounts detected for 96(Ti-45Nb)-4Ga and 92 (Ti-45Nb)-8Ga are 1.69 ($\pm$ 0.38) and 2.88 ($\pm$ 0.04) ppb (or µg/L), respectively (**Fig. S2**).

4. Discussion

Poor wear resistance of β-Ti alloys is still a major limiting factor for their real use as biomedical implant materials. Thus, the current work aimed to evaluate the influence of Ga addition (4 and 8 wt%) to the β-type Ti-45Nb alloy on the tribocorrosion response and eventual Ga ion release associated with wear-accelerated corrosion.

The addition of Ga up to 8 wt% to the binary Ti-45Nb retains single β-phase microstructure and does not lead to the formation of secondary phases (α'' or ω), which might significantly increase the Young's modulus [49]. On the other hand, Ga addition slightly increases the Young's modulus, measured by pulse-echo ultrasonic method, from 63 GPa of Ti-45Nb to 69 and 79 GPa for 96(Ti-45Nb)-4Ga and 92 (Ti-45Nb)-8Ga, respectively (Table 1). This effect is mainly attributed to a strengthening effect exerted by the presence of Ga atoms in the bcc lattice [14]. Meanwhile, Ga addition has a positive effect on Vickers microhardness, with values of 226 and 232 $HV_{0.1}$, which indicate an increase of ~ 54, 58% with respect to the reference Ti-45Nb.

The addition of Ga to Ti-45Nb has a positive effect on corrosion and tribocorrosion response. Lower repassivation time constants (t_{repass}) are determined from the OCP curves (Fig. 4) for the two (100-x)(Ti-45Nb)-xGa alloys, indicating a faster transient to reach pre-sliding conditions, followed by Ti-45Nb and Ti-6Al-4V ELI. During the potentiodynamic studies, and despite the limitations of this method, lower j_{pass} is obtained for 96(Ti-45Nb)-4Ga (4.38 µA/cm^2) and 92(Ti-45Nb)-8Ga (3.48 µA/cm^2) compared to Ti-45Nb. In this case, Ti-6Al-4V ELI, which exhibited the lowest j_{pass} (2.47 µA/cm^2) during corrosion studies, showed the highest t_{repass} during tribocorrosion, pointing towards a slower repassivation kinetic during mechanical disruption. In general, Ti alloys exhibit meagre surface oxide damage even up to 4–5 V during potentiodynamic polarization in simulated body fluids [43]. This is consistent with several studies where the repassivation trend during corrosion is not in-line with that of wear-accelerated corrosion [50]. Among the Ga-containing alloys, 92(Ti-45Nb)-8Ga shows an increasing drift trend towards higher potential during tribocorrosion (Fig. 4**a**), suggesting a pronounced repassivation state with less depassivation, even during mechanical degradation. Interestingly, tests under applied anodic potential show great differences between Ti-6Al-4V ELI (α + β) and the three Ti-Nb (β) alloys, with large current fluctuations for the latter. Being the current before sliding at the applied anodic potential below 10 nA for all the alloys, it is assumed that the wear current (i_{wear}), as reported in Table 3 and which is 3–5 orders of magnitude higher, is mainly flowing through the wear track during sliding. There is no significant difference in i_{wear} of the three Ti-Nb alloys and the influence of alloys' chemical composition on the measured current is also not significant. The significantly lower i_{wear} of the Ti-6Al-4V ELI indicates that this alloy undergoes lower anodic dissolution during sliding. Feyzi et al. [45] studied the tribocorrosion behavior of Ti-6Al-4V in PBS solution and also observed similar current fluctuations, which increased with the potential level and proportionally with the applied load. The periodic film removal (depassivation) and formation (repassivation) keeps the current at relatively high values. Similar behavior in other passive systems was observed by other authors: α + β-Ti and β-Ti [24,25], CoCrMo [42], stainless steels [30,51,52], Zr-based alloys [53].

The large fluctuations observed in COF evolution with time during sliding (Fig. 4**b**) for the β-Ti-Nb alloys are mainly attributed to the

poorer wear resistance and lower microhardness than α + β Ti-6Al-4V ELI. The observed phenomenon can also be attributed to the large amount of wear debris produced during the sliding tests, particularly for the three Ti-Nb-based alloys, which act as third bodies, thus enhancing wear and wear-accelerated corrosion. COFs in this work are comparable to those of similar alloys tested in similar conditions reported in the literature: Hacisalihoglu et al. [24] studied in Kokubo's solution a series of Ti-based alloys, among which Ti-6Al-4V and Ti-45Nb. They observed COF values in the range 0.11 ÷ 0.22, obtained using a ball-on-flat tribometer under an initial normal load of 2 N against an alumina ball (R = 6 mm), which is less than half than the load applied in this work (5 N); initial contact pressures are slightly higher in their work, however the frictional force depends also on sliding velocity, real contact area and lubrication. Considerable fluctuations of COFs during wear in this work are also observed and it is attributed to the depassivation products caused by rubbing. Guiñon Pina et al. [25] observed COF values in the range of 0.59 ÷ 0.71 in tribocorrosion tests in PBS solution on a series of Ti-30Nb-xSn alloys sliding against an alumina ball (R = 6 mm) under an applied normal load of 5 N.

During tribocorrosion contribution analysis (Table 4), mechanical material loss (V_{mech}) is dominant for all tested Ti alloys. In comparison, the three β-Ti alloys display higher V_{mech} compared to α + β Ti6Al-4V. Mechanical wear as the weak point during tribocorrosion has been well reported for Ti-6Al-4V [54]. No significant differences among the three β-Ti-Nb-based alloys can be observed in the computed volumes due to wear-accelerated corrosion (V_{wac}), except for Ti-6Al-4V ELI, indicating that Ga has little to no effect on the overall electrochemical response. It is important to pinpoint that the addition of Ga to Ti-45Nb does improve wear resistance as it can be seen from the total volumetric wear data (V_{tot}), and therefore mechanical wear contribution (V_{mech}), of the wear tracks. According to Archard's law [55], the material loss is inversely proportional to the hardness of the material, which implies that materials with high hardness exhibit low volume loss. The alloys under investigation have significantly different microhardness, and the experimental sliding data shown here correlates well with Archard's law (Fig. 7). The lowest wear loss is observed for the Ti-6Al-4V ELI possessing the highest microhardness (354 $HV_{0.1}$), while Ti-45Nb exhibits the lowest microhardness (147 $HV_{0.1}$) and the greatest volume loss, the two (100-x)(Ti-45Nb)-xGa alloys situate between these two (226, 232 $HV_{0.1}$). We can state that wear resistance is mainly controlled by hardness, i.e. microstructural effects, and alloy composition. This is also supported by the tribocorrosion studies of Cvijović-Alagić et al. [56] on Ti-6Al-4V ELI in different states. They observed that the total wear loss of a two-phase microstructure α + β Ti-6Al-4V ELI is almost two times
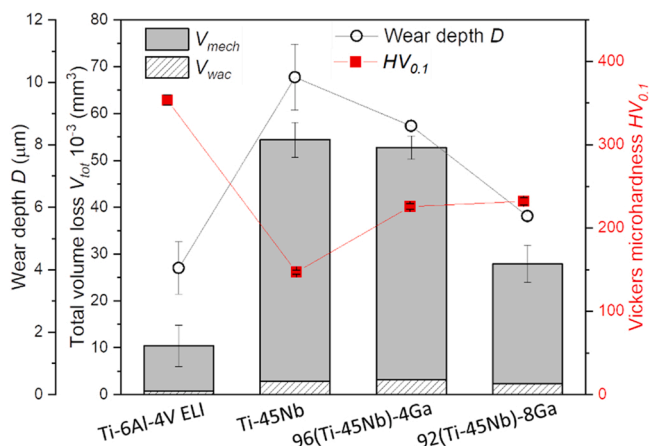

Fig. 7. Variation per alloy of total volume loss (V_{tot}) with the contributions of mechanical wear (V_{mech}), wear-accelerated corrosion (V_{wac}) and wear depth (D) measured by 3D optical profilometry, plotted with Vickers microhardness ($HV_{0.1}$).

higher than that of martensitic Ti-6Al-4V ELI alloy, because Ti martensites are relatively soft, if compared for example to martensites in steel. Besides, in this work volumetric wear data are well supported by the microstructural investigations of the wear tracks (Fig. 6). Oxidative wear consists of surface oxide islands which are periodically formed and mechanically worn away; as such, they are not protective and resulting wear becomes severe. In the present investigation, the surface of the alloys during the tribocorrosion tests is under continuous contact sliding, resulting in reduced wear resistance, due to their inability in forming a thicker protective oxide layer. Consequently, total wear loss is mainly determined by the hardness, and sub-surface strain deformation could also occur during sliding in the near surface zone, increasing the scope for further investigation. The processes occurring during wear are well described by Long and Rack [57], where they show the detachment mechanism of debris in a Ti-35Nb-8Zr-5Ta alloy is related to the plastic deformation of superficial layers below the wear track. Overall, the wear track analysis suggests that wear is mainly due to plastic deformation, abrasive wear, delamination wear and adhesive wear.

ICP-MS studies on the test solutions reveal the presence of Ga(III) ions, indicating minimal dissolution during wear tests. Amounts released are well below ($\sim$ 4 orders of magnitude) the limits reported by Chandler et al. [58], who found no cytotoxicity on L929 mouse fibroblasts at Ga(III) contents up to 1 mmol/L (70 mg/L). At the released concentrations, Ga does not appear to be cytotoxic either to osteoclasts or osteoblasts [59,60], however, an eventual bactericidal activity against pathogens is expected based on values from other works [48,61], therefore further studies are needed in this direction. Moreover, in vitro studies showed that Ga ions exhibit antiosteoclastic effects without negatively impacting osteoblasts, which therefore makes Ga a potential candidate for osteoporosis treatment [62]. The low amounts of ions released during tribocorrosion tests from the Ti-Nb-based alloys can be attributed to their single-phase microstructure, i.e. solid solution. In such a state, elements are uniformly distributed in the alloy matrix and uniform corrosion tends to take place, instead of localized corrosion. In the investigated potential-pH range, all three elements (Ti, Nb, Ga) form stable and passive oxide films, which contribute to the low corrosion rates. Moreover, the presence of Ga can lead to the formation of Ga—O—Ga bonds in the oxide layer, thus increasing durability, and therefore wear resistance [48]. Further enquiries on the surface state to confirm the previous statement are currently ongoing. The possibility of using these novel Ti-Nb-Ga alloys for biomedical load-bearing implant applications represents a promising alternative to Ti-6Al-4V. The absence of toxic elements such as Al and V would render these alloys safer to be used in the human body. Besides, these β-type alloys exhibit the advantage of having low Young's modulus (E of the two (100-x)(Ti-45Nb)-xGa alloys is 29–37% lower than E of Ti-6Al-4V ELI), thus reducing the stress shielding phenomenon. Further studies are necessary for an eventual real clinical application: in vitro tribo-electrochemical testing, including fretting conditions, at body temperature, in a more complex medium and in presence of organic molecules, salts and cells.

5. Conclusions

In the present study, microstructure, mechanical properties and tribocorrosion behavior of novel β-type (100-x)(Ti-45Nb)-xGa alloys (x = 4, 8 wt%), compared to medical grade α + β Ti-6Al-4V ELI, were investigated and the following conclusions can be drawn.

The three Ti-Nb-based alloys consist of a bcc β-phase microstructure with equiaxed β-grains. Addition of the alloying element Ga in 4 wt% and 8 wt% to Ti-45Nb leads to an increase in microhardness (226, 232 $HV_{0.1}$, respectively) of $\sim$ 54, 58% and in E (69.4, 79.1 GPa, respectively) of $\sim$ 10, 26%. The tested alloys exhibit similar potentiodynamic behavior in PBS solution. Under sliding conditions, all alloys tend to repassivate and similar tribocorrosion mechanisms occur; plastic deformation, abrasive wear, delamination wear and adhesive wear. Addition of Ga increased wear resistance of Ti-45Nb. The two Ti-Nb-Ga

alloys repassivate more rapidly than Ti-6Al-4V ELI alloy. Existing models accurately predicted the tribo-electrochemical response of the studied alloys. The low modulus β-type 92(Ti-45Nb)-8Ga alloy displays the best combination of both corrosion and wear resistance, with a repassivation time constant of 17.3 s and spontaneous tendency to repassivate even during mechanical degradation.

The present study represents, from a mechanistic point of view, a significant advance: the tribocorrosion mechanisms of these original single β-phase (100-x)(Ti-45Nb)-xGa alloys in a simple simulated body fluid were disclosed.

Declaration of Competing Interest

The authors declare the following financial interests/personal relationships which may be considered as potential competing interests. Ludovico Andrea Alberta reports financial support was provided by European Commission.

Data Availability

Data will be made available on request.

Statement of originality

The authors declare that the work with the title **Tribocorrosion behavior of β-type Ti-Nb-Ga alloys in a physiological solution** is original and has not been published elsewhere, nor is it currently under consideration for publication elsewhere.

Appendix A. Supporting information

Supplementary data associated with this article can be found in the online version at doi:10.1016/j.triboint.2023.108325.

References

[1] Inan-Eroglu E, Ayaz A. Is aluminum exposure a risk factor for neurological disorders. J Res Med Sci 2018;23:51. https://doi.org/10.4103/jrms.JRMS_921_17.

[2] Gomes CC, Moreira LM, Santos VJSV, Ramos AS, Lyon JP, Soares CP, et al. Assessment of the genetic risks of a metallic alloy used in medical implants. Genet Mol Biol 2011;34:116–21. https://doi.org/10.1590/S1415-47572010005000118.

[3] Ali S, Abdul Rani AM, Baig Z, Ahmed SW, Hussain G, Subramaniam K, et al. Biocompatibility and corrosion resistance of metallic biomaterials. Corros Rev 2020;38:381–402. https://doi.org/10.1515/corrrev-2020-0001.

[4] Bönisch M, Calin M, Waitz T, Panigrahi A, Zehetbauer M, Gebert A, et al. Thermal stability and phase transformations of martensitic Ti–Nb alloys. Sci Technol Adv Mater 2013;14:055004. https://doi.org/10.1088/1468-6996/14/5/055004.

[5] Gostin PF, Helth A, Voss A, Sueptitz R, Calin M, Eckert J, et al. Surface treatment, corrosion behavior, and apatite-forming ability of Ti-45Nb implant alloy. J Biomed Mater Res - Part B Appl Biomater 2013;101 B:269–78. https://doi.org/10.1002/jbm.b.32836.

[6] Calin M, Helth A, Gutierrez Moreno JJ, Bönisch M, Brackmann V, Giebeler L, et al. Elastic softening of β-type Ti-Nb alloys by indium (In) additions. J Mech Behav Biomed Mater 2014;39:162–74. https://doi.org/10.1016/j.jmbbm.2014.07.010.

[7] Pilz S, Geissler D, Calin M, Eckert J, Zimmermann M, Freudenberger J, et al. Thermomechanical processing of In-containing β-type Ti-Nb alloys. J Mech Behav Biomed Mater 2018;79:283–91. https://doi.org/10.1016/j.jmbbm.2017.12.028.

[8] Geetha M, Singh AK, Asokamani R, Gogia AK. Ti based biomaterials, the ultimate choice for orthopaedic implants - a review. Prog Mater Sci 2009;54:397–425. https://doi.org/10.1016/j.pmatsci.2008.06.004.

[9] Hanada S, Ozaki T, Takahashi E, Watanabe S, Yoshimi K, Abumiya T. Composition dependence of Young's Modulus in beta titanium binary alloys. Mater Sci Forum 2003;426–432:3103–8. https://doi.org/10.4028/www.scientific.net/MSF.426-432.3103.

[10] Sarraf M, Rezvani Ghomi E, Alipour S, Ramakrishna S, Liana Sukiman N. A state-of-the-art review of the fabrication and characteristics of titanium and its alloys for biomedical applications. Bio-Des Manuf 2022;5:371–95. https://doi.org/10.1007/s42242-021-00170-3.

[11] Lemire JA, Harrison JJ, Turner RJ. Antimicrobial activity of metals: Mechanisms, molecular targets and applications. Nat Rev Microbiol 2013;11:371–84. https://doi.org/10.1038/nrmicro3028.

[12] Minandri F, Bonchi C, Frangipani E, Imperi F, Visca P. Promises and failures of gallium as an antibacterial agent. Future Microbiol 2014;9:379–97. https://doi.org/10.2217/fmb.14.3.

[13] Cochis A, Azzimonti B, Chiesa R, Rimondini L, Gasik M. Metallurgical gallium additions to titanium alloys demonstrate a strong time-increasing antibacterial activity without any cellular toxicity. ACS Biomater Sci Eng 2019;5:2815–20. https://doi.org/10.1021/acsbiomaterials.9b00147.

[14] Alberta LA, Vishnu J, Hariharan A, Pilz S, Gebert A, Calin M. Novel low modulus beta-type Ti–Nb alloys by gallium and copper minor additions for antibacterial implant applications. J Mater Res Technol 2022;20:3306–22. https://doi.org/10.1016/j.jmrt.2022.08.111.

[15] Kim KT, Eo MY, Nguyen TTH, Kim SM. General review of titanium toxicity. Int J Implant Dent 2019;5. https://doi.org/10.1186/s40729-019-0162-x.

[16] Vieira AC, Ribeiro AR, Rocha LA, Celis JP. Influence of pH and corrosion inhibitors on the tribocorrosion of titanium in artificial saliva. Wear 2006;261:994–1001. https://doi.org/10.1016/j.wear.2006.03.031.

[17] Vishnu J, Manivasagam G. Surface modification and biological approaches for tackling titanium wear-induced aseptic loosening. J Bio- Tribo-Corros 2021;7:1–19. https://doi.org/10.1007/s40735-021-00474-y.

[18] Haynes DR, Rogers SD, Hay S, Pearcy MJ, Howie DW. The differences in toxicity and release of bone-resorbing mediators induced by titanium and cobalt-chromium-alloy wear particles. J Bone Jt Surg - Ser A 1993;75:825–34. https://doi.org/10.2106/00004623-199306000-00004.

[19] Vishnu J, Ansheed AR, Hameed P, Praveenkumar K, Pilz S, Alberta LA, et al. Insights into the surface and biocompatibility aspects of laser shock peened Ti-22Nb alloy for orthopedic implant applications. Appl Surf Sci 2022;586:152816. https://doi.org/10.1016/j.apsusc.2022.152816.

[20] Alam MO, Haseeb ASMA. Response of Ti-6Al-4V and Ti-24Al-11Nb alloys to dry sliding wear against hardened steel. Tribol Int 2002;35:357–62. https://doi.org/10.1016/S0301-679X(02)00015-4.

[21] Martin É, Azzi M, Salishchev GA, Szpunar J. Influence of microstructure and texture on the corrosion and tribocorrosion behavior of Ti-6Al-4V. Tribol Int 2010;43:918–24. https://doi.org/10.1016/j.triboint.2009.12.055.

[22] Feyzi M, Fallahnezhad K, Taylor M, Hashemi R. What role do normal force and frequency play in the tribocorrosion behaviour of Ti-6Al-4V alloy? Tribol Int 2022;172:107634. https://doi.org/10.1016/j.triboint.2022.107634.

[23] Çaha I, Alves A, Chirico C, Pinto A, Tsipas S, Gordo E, et al. Corrosion and tribocorrosion behavior of Ti-40Nb and Ti-25Nb-5Fe alloys processed by powder metallurgy. Met Mater Trans A Phys Met Mater Sci 2020;51:3256–67. https://doi.org/10.1007/s11661-020-05757-6.

[24] Hacisalihoglu I, Samancioglu A, Yildiz F, Purcek G, Alsaran A. Tribocorrosion properties of different type titanium alloys in simulated body fluid. Wear 2015;332–333:679–86. https://doi.org/10.1016/j.wear.2014.12.017.

[25] Pina VG, Dalmau A, Devesa F, Amigó V, Muñoz AI. Tribocorrosion behavior of beta titanium biomedical alloys in phosphate buffer saline solution. J Mech Behav Biomed Mater 2015;46:59–68. https://doi.org/10.1016/j.jmbbm.2015.02.016.

[26] Alberta LA, Fortouna Y, Vishnu J, Pilz S, Gebert A, Lekka C, et al. Effects of Ga on the structural, mechanical and electronic properties of β-Ti45Nb alloy by experiments and Ab initio calculations. SSRN Electron J 2022. https://doi.org/10.2139/ssrn.4264244.

[27] Wu SJ, Chin PC, Liu H. Measurement of elastic properties of brittle materials by ultrasonic and indentation methods. Appl Sci 2019;9. https://doi.org/10.3390/app9102067.

[28] Impergre A, Trunfio-Sfarghiu AM, Der-Loughian C, Brizuela L, Mebarek S, Ter-Ovanessian B, et al. Tribocorrosion of polyethylene/cobalt contact combined with real-time fluorescence assays on living macrophages: development of a multidisciplinary biotribology device. Biotribology 2019;18:100091. https://doi.org/10.1016/j.biotri.2019.100091.

[29] Stemp M, Mischler S, Landolt D. The effect of contact configuration on the tribocorrosion of stainless steel in reciprocating sliding under potentiostatic control. Corros Sci 2003;45:625–40. https://doi.org/10.1016/S0010-938X(02)00136-1.

[30] Dalbert V, Mary N, Normand B, Verdu C, Saedlou S. In situ determinations of the wear surfaces, volumes and kinetics of repassivation: contribution in the understanding of the tribocorrosion behaviour of a ferritic stainless steel in various pH. Tribol Int 2020;150:106374. https://doi.org/10.1016/j.triboint.2020.106374.

[31] Stojadinović J, Bouvet D, Declercq M, Mischler S. Effect of electrode potential on the tribocorrosion of tungsten. Tribol Int 2009;42:575–83. https://doi.org/10.1016/j.triboint.2008.04.009.

[32] Mischler S, Spiegel A, Stemp M, Landolt D. Influence of passivity on the tribocorrosion of carbon steel in aqueous solutions. Wear 2001;250–251:1295–307. https://doi.org/10.1016/s0043-1648(01)00754-2.

[33] Cao S, Guadalupe Maldonado S, Mischler S. Tribocorrosion of passive metals in the mixed lubrication regime: theoretical model and application to metal-on-metal artificial hip joints. Wear 2015;324–325:55–63. https://doi.org/10.1016/j.wear.2014.12.003.

[34] Godley R, Starosvetsky D, Gotman I. Corrosion behavior of a low modulus β-Ti-45%Nb alloy for use in medical implants. J Mater Sci Mater Med 2006;17:63–7. https://doi.org/10.1007/s10856-006-6330-6.

[35] Vieira AC, Rocha LA, Papageorgiou N, Mischler S. Mechanical and electrochemical deterioration mechanisms in the tribocorrosion of Al alloys in NaCl and in NaNO3 solutions. Corros Sci 2012;54:26–35. https://doi.org/10.1016/j.corsci.2011.08.041.

[36] Helth A, Pilz S, Kirsten T, Giebeler L, Freudenberger J, Calin M, et al. Effect of thermomechanical processing on the mechanical biofunctionality of a low modulus Ti-40Nb alloy. J Mech Behav Biomed Mater 2017;65:137–50. https://doi.org/10.1016/j.jmbbm.2016.08.017.

[37] Kumar S, Sankara Narayanan TSN. Electrochemical characterization of β-Ti alloy in Ringer's solution for implant application. J Alloy Compd 2009;479:699–703. https://doi.org/10.1016/j.jallcom.2009.01.036.

[38] Sidhu SS, Singh H, Gepreel MAH. A review on alloy design, biological response, and strengthening of β-titanium alloys as biomaterials. Mater Sci Eng C 2021:121. https://doi.org/10.1016/j.msec.2020.111661.

[39] Bai Y, Deng Y, Zheng Y, Li Y, Zhang R, Lv Y, et al. Characterization, corrosion behavior, cellular response and in vivo bone tissue compatibility of titanium-niobium alloy with low Young's modulus. Mater Sci Eng C 2016;59:565–76. https://doi.org/10.1016/j.msec.2015.10.062.

[40] Gebert A, Oswald S, Helth A, Voss A, Gostin PF, Rohnke M, et al. Effect of indium (In) on corrosion and passivity of a beta-type Ti-Nb alloy in Ringer's solution. Appl Surf Sci 2015;335:213–22. https://doi.org/10.1016/j.apsusc.2015.02.058.

[41] Yazdi R, Ghasemi HM, Abedini M, Monshi M. Interplay between mechanical wear and electrochemical corrosion during tribocorrosion of oxygen diffusion layer on Ti-6Al-4V in PBS solution. Appl Surf Sci 2020;518:146048. https://doi.org/10.1016/j.apsusc.2020.146048.

[42] Guadalupe Maldonado S, Mischler S, Cantoni M, Chitty WJ, Falcand C, Hertz D. Mechanical and chemical mechanisms in the tribocorrosion of a Stellite type alloy. Wear 2013;308:213–21. https://doi.org/10.1016/j.wear.2013.04.007.

[43] Ren P, Meng H, Xia Q, Zhu Z, He M. Influence of seawater depth and electrode potential on the tribocorrosion of Ti6Al4V alloy under the simulated deep-sea environment by in-situ electrochemical technique. Corros Sci 2021;180:109185. https://doi.org/10.1016/j.corsci.2020.109185.

[44] Mischler S, Spiegel A, Landolt D. The role of passive oxide films on the degradation of steel in tribocorrosion systems. Wear 1999;225–229:1078–87. https://doi.org/10.1016/S0043-1648(99)00056-3.

[45] Feyzi M, Fallahnezhad K, Taylor M, Hashemi R. The tribocorrosion behaviour of Ti-6Al-4 V alloy: the role of both normal force and electrochemical potential. Tribol Lett 2022;70:1–16. https://doi.org/10.1007/s11249-022-01624-0.

[46] Espallargas N, Torres C, Muñoz AI. A metal ion release study of CoCrMo exposed to corrosion and tribocorrosion conditions in simulated body fluids. Wear 2015;332–333:669–78. https://doi.org/10.1016/j.wear.2014.12.030.

[47] Li Y, Wong C, Xiong J, Hodgson P, Wen C. Cytotoxicity of titanium and titanium alloying elements. J Dent Res 2010;89:493–7. https://doi.org/10.1177/0022034510363675.

[48] Łapa A, Cresswell M, Campbell I, Jackson P, Goldmann WH, Detsch R, et al. Gallium- and cerium-doped phosphate glasses with antibacterial properties for medical applications. Adv Eng Mater 2020;22:1901577. https://doi.org/10.1002/adem.201901577.

[49] Abdel-Hady Gepreel M, Niinomi M. Biocompatibility of Ti-alloys for long-term implantation. J Mech Behav Biomed Mater 2013;20:407–15. https://doi.org/10.1016/j.jmbbm.2012.11.014.

[50] Khan MA, Williams RL, Williams DF. The corrosion behaviour of Ti–6Al–4V, Ti–6Al–7Nb and Ti–13Nb–13Zr in protein solutions. Biomaterials 1999;20:631–7. https://doi.org/10.1016/S0142-9612(98)00217-8.

[51] Dalbert V, Mary N, Normand B, Verdu C, Douillard T, Saedlou S. The effects of microstructures and repassivation kinetics on the tribocorrosion resistance of ferrite and ferrite-martensite stainless steels. Wear 2019;420–421:245–56. https://doi.org/10.1016/j.wear.2018.10.023.

[52] Mary N, Ter-Ovanessian B, Normand B. Growth mechanism and repassivation kinetic determinations on stainless steel under sliding: Role of the solution pH and dissolved oxygen concentration. Wear 2020;460–461:203478. https://doi.org/10.1016/j.wear.2020.203478.

[53] Priya R, Mallika C, Mudali UK. Wear and tribocorrosion behaviour of 304L SS, Zr-702, Zircaloy-4 and Ti-grade2. Wear 2014;310:90–100. https://doi.org/10.1016/j.wear.2013.11.051.

[54] Namus R, Rainforth WM. The influence of cathodic potentials on the surface oxide layer status and tribocorrosion behaviour of Ti6Al4V and CoCrMo alloys in simulated body fluid. Biotribology 2022;30:100212. https://doi.org/10.1016/j.biotri.2022.100212.

[55] Archard JF. Contact and rubbing of flat surfaces. J Appl Phys 1953;24:981–8. https://doi.org/10.1063/1.1721448.

[56] Cvijović-Alagić I, Cvijović Z, Mitrović S, Panić V, Rakin M. Wear and corrosion behaviour of Ti-13Nb-13Zr and Ti-6Al-4V alloys in simulated physiological solution. Corros Sci 2011;53:796–808. https://doi.org/10.1016/j.corsci.2010.11.014.

[57] Long M, Rack HJ. Subsurface deformation and microcrack formation in Ti-35Nb-8Zr-5Ta-O(x) during reciprocating sliding wear. Mater Sci Eng C 2005;25:382–8. https://doi.org/10.1016/j.msec.2005.01.027.

[58] Chandler JE, Messer HH, Ellender G. Cytotoxicity of gallium and indium ions compared with mercuric ion. J Dent Res 1994;73:1554–9. https://doi.org/10.1177/00220345940730091101.

[59] Yamaguchi S, Nath S, Sugawara Y, Divakarla K, Das T, Manos J, et al. Two-in-one biointerfaces—Antimicrobial and bioactive nanoporous gallium titanate layers for titanium implants. Nanomaterials 2017:7. https://doi.org/10.3390/nano7080229.

[60] Verron E, Masson M, Khoshniat S, Duplomb L, Wittrant Y, Baud'Huin M, et al. Gallium modulates osteoclastic bone resorption in vitro without affecting osteoblasts. Br J Pharm 2010;159:1681–92. https://doi.org/10.1111/j.1476-5381.2010.00665.x.

[61] Kurtjak M, Vukomanović M, Krajnc A, Kramer L, Turk B, Suvorov D. Designing Ga (iii)-containing hydroxyapatite with antibacterial activity. RSC Adv 2016;6:112839–52. https://doi.org/10.1039/c6ra23424k.

[62] Verron E, Bouler JM, Scimeca JC. Gallium as a potential candidate for treatment of osteoporosis. Drug Discov Today 2012;17:1127–32. https://doi.org/10.1016/j.drudis.2012.06.007.